Deep-UV microsphere projection lithography

Alireza Bonakdar, Mohsen Rezaei, Robert L. Brown, Vala Fathipour, Eric Dexheimer, Sung Jun Jang, and Hooman Mohseni*

Bio-Inspired Sensors and Optoelectronics Laboratory (BISOL), Department of Electrical Engineering and Computer Science, Northwestern University, Evanston, Illinois 60208, USA
**Corresponding author: hmohseni@northwestern.edu*

Received April 1, 2015; revised April 24, 2015; accepted April 28, 2015; posted April 30, 2015 (Doc. ID 236973); published May 21, 2015

In this Letter, we present a single-exposure deep-UV projection lithography at 254-nm wavelength that produces nanopatterns in a scalable area with a feature size of 80 nm. In this method, a macroscopic lens projects a pixelated optical mask on a monolayer of hexagonally arranged microspheres that reside on the Fourier plane and image the mask's pattern into a photoresist film. Our macroscopic lens shrinks the size of the mask by providing an imaging magnification of $\sim 1.86 \times 10^4$, while enhancing the exposure power. On the other hand, microsphere lens produces a sub-diffraction limit focal point—a so-called photonic nanojet—based on the near-surface focusing effect, which ensures an excellent patterning accuracy against the presence of surface roughness. Ray-optics simulation is utilized to design the bulk optics part of the lithography system, while a wave-optics simulation is implemented to simulate the optical properties of the exposed regions beneath the microspheres. We characterize the lithography performance in terms of the proximity effect, lens aberration, and interference effect due to refractive index mismatch between photoresist and substrate.

OCIS codes: (110.5220) Photolithography; (110.4235) Nanolithography; (220.4241) Nanostructure fabrication; (210.4770) Optical recording.
http://dx.doi.org/10.1364/OL.40.002537

Microsphere photolithography is an attractive method to fabricate nanopatterns on large areas. In this type of photolithography, microspheres are used as microlenses to focus UV light into a photoresist film underneath the spheres [1] that can be used to produce arbitrary patterns [2,3] or to focus on a material that can be patterned by laser ablation [4]. The focal spot of microspheres has a jet-like shape—a near-field focusing effect, where an elongated beam forms immediately beneath the microsphere [5]. In contrast to microlens fabrication, chemically synthesized microspheres do not require any microfabrication process resulting in a lower cost and a greater available of materials. In addition, the size of microspheres are available in a wide range from ~10 nm to several 100 μm diameter with a standard deviation of less than 2%. These properties make microsphere lenses valuable as they are compatible with a variety of optoelectronic applications [6–10].

To expand the capability of microsphere photolithography, it is necessary to achieve feature sizes below 100 nm, particularly to access resonant responses in the near IR and visible regions of the spectrum. However, the width of the focal point limits the feature size. Reducing the size of the nanojet can be achieved by utilizing deep/extreme UV wavelength sources. Particularly, the optical path of microspheres is short enough to avoid optical absorption that most materials exhibit in UV region. Recently, we achieved a 80-nm feature size via microsphere photolithography by replacing common 365-nm i-line source with 254-nm-deep UV (DUV) source [11]. Figure 1 shows the highly elongated nanopillars of photoresist fabricated via DUV microsphere photolithography using 2-μm spheres on silicon substrate that a 1-μm-thick layer of SiO_2 has been deposited as an anti-reflection coating film to reduce interference effects.

In this Letter, we extend DUV microsphere photolithography to produce arbitrary nanopatterns by incorporating a projection optical system. In this method, a macroscopic lens acts as an objective lens and projects a mask onto a monolayer of microspheres that act as imaging lenses at the Fourier plane of the objective lens. Figure 2(a) shows a homemade projection lithography setup inside a broadband DUV chamber. A mechanical shutter is used to set accurate and stable exposure time slots. The schematic is shown in Fig. 2(b). It is composed of a DUV filter that transmits 254-nm light through a stack of two diffusers. The diffuser increases illumination uniformity and creates a wider angular distribution of light passing through the mask's openings. The optical mask is pixelated to compensate for the proximity effect and correct aberrations from the microspheres. Another advantage of the pixelated mask is to have a uniform lithography exposure duration. The two plano–convex (PCX) lenses serve as an objective lens that maps the mask openings on an array of microspheres. Although, a single spherical lens is enough to map the mask on the microsphere array, the trade-off between the lens power and lens aberration leads to a compromise between the pattern size underneath the microsphere and the size of

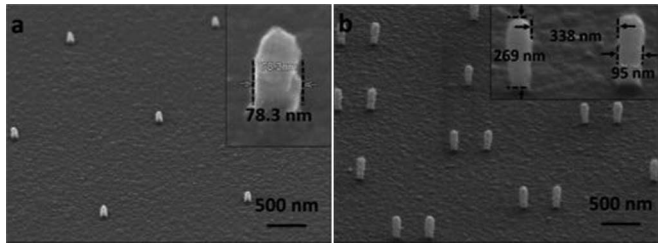

Fig. 1. (a) Achieving feature size of sub-80-nm using 254-nm-wavelength DUV source in a microsphere photolithography. The microsphere size is 2 μm. (b) DUV microsphere photolithography is susceptible for generic nanopatterning. An array of double-pillar photoresist fabricated by DUV tilted exposure microsphere photolithography. Pillars shows high-aspect ratio without bending.

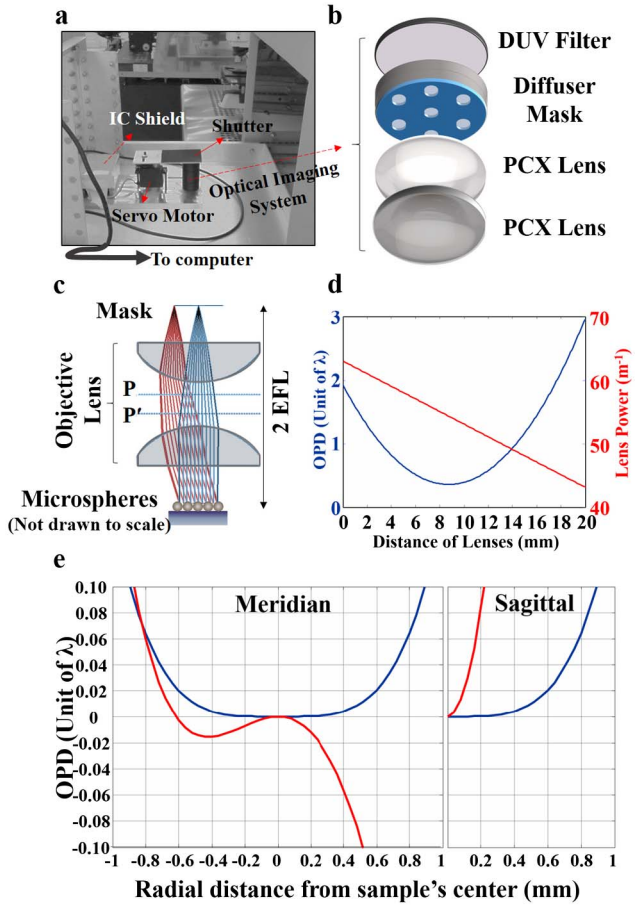

Fig. 2. (a) Homemade DUV lithography setup inside a broadband DUV chamber. A shutter is controlled by a computer to set the stable exposure time slots. (b) Arrangement of the optical system. A DUV filter passes light with 254-nm wavelength from a broadband source. A stack of two diffusers is served to increase illumination uniformity and to enrich angular distribution of light passing through the mask. The two lenses create an objective lens system that maps the mask openings on an array of microspheres. The mask and microsphere array are placed at the effective focal points of the objective lens system. (c) Ray-tracing simulation (WinLens3D) of the objective lens system that projects two points of a mask on an array of microsphere imagining lenses. The objective lens is composed of two PCX lenses that are situated for minimized aberration. (d) Graphs of optical path difference and magnification as a function of two PCX lenses. (e) OPD across the sample for meridian and sagittal beams originated from center (blue line) and 5 mm (red line) away from center of the mask. Note the center of sample is coincided with center of optics.

aberration-free region of the sample. To resolve this limitation, one can choose more sophisticated but relatively costly lenses such as an aspheric lens to have high lens power with small aberration. Fortunately, in many situations, a lens system with an accurate design can meet these criteria. Here, we designed an objective lens composed of two PCX lenses with flat-sides facing toward the mask and sample. For a thick lens or a system of lenses, the effective focal length (EFL) is defined as the distance from the focal point to the principle plane [shown as dashed lines P and P' in Fig. 2(c)] for each side of the lens system. Both the mask and microspheres are placed at the opposite EFLs of the objective lens system. The optical design of the lithography system involves both ray optics for the objective lens ($\gg \lambda$) and wave optics for imaging lens ($\sim\lambda$) due to the significant dimension contrast. Figure 2(c) illustrates the ray-tracing simulation of two PCX fused silica lenses where they are placed in an optimum distance to produce minimum aberration. The magnification of the system is the ratio of the EFL of the objective lens to the focal length of the microsphere, which is the microsphere radius. The coverage area on the sample is limited to the overlap of beams from farthest openings of the mask. For the case of aberration-free ray tracing, the coverage area has a diameter of $d_{\text{sample}} = d_{\text{lens}} - d_{\text{mask}}$, where d_{lens} and d_{mask} are lens and mask diameters, respectively. In practice, lens aberration reduces the coverage area. Figure 2(d) depicts the ray-tracing simulation result of the optical path difference (OPD) across the Fourier plane of the objective lens. It is defined as the relative phase distortion between the rays arriving on the sample's surface with respect to the one arriving at the center of the sample. The minimum OPD is for a distance of 9 mm with a lens power of 54 m^{-1}, while each PCX lens by itself has a lens power of 31 m^{-1} as depicted in Fig. 2(d). OPD is a useful parameter to extract an effective coverage area with insignificant aberration. Figure 2(e) illustrates aberration across the sample for two beams originating from the mask's center and 5 mm away from the mask's center. Both meridian and sagittal beams are considered for full evaluation of OPD. Setting the maximum OPD to 0.1λ, an effective coverage area with negligible aberration has a diameter of ~2 mm. Since the mask is positioned at the focal point, the image of the objective lens is decomposed into a series of weighted planewaves with different angles of incidence. An objective lens with effective focal length of EFL converts the alike spherical beam from a point on the mask (with a radial distance P_{mask} from center of mask) into a set of parallel beams with angle equal to $\theta = \tan^{-1}(P_{\text{mask}}/EFL)$. The pillar position under a microsphere with a radius of R_{sphere} is related to the angle of beam by $P_{\text{pillar}} = R_{\text{sphere}} \tan(\theta) = R_{\text{sphere}}(P_{\text{mask}}/\text{EFL})$. Note that the magnification of the lithography system is $M = \text{EFL}/R_{\text{sphere}}$. Thus, one can relate mask position to pillar position through $P_{\text{pillar}} = P_{\text{mask}}/M$. Therefore, a wave optics simulation (FDTD Lumerical solution) is needed to evaluate the formation of a photonic nanojet with different angles of incidence as shown in Fig. 3(a). Since, in the experiment, the deposited photoresist has a measured thickness of 280 nm (measured by spectroscopic ellipsometry) on a glass slide substrate, in FDTD simulation, we assume the same conditions. Note that the beams with a higher angle of incidence produce photonic nanojet with less intensity and larger bending due to microsphere aberration. In addition, in a practical setup, it is always difficult to produce an incident beam with uniform intensity. Therefore, wider opening size is necessary to compensate less intensity toward the edge of the mask. Through the adjustment of intensity for each angle, one can resolve pillars with a broad range of angles over a large area. In addition, the refractive index contrast between the photoresist and glass substrate produces interference patterns along walls of the photoresist pillars. Although interference effect can be useful to induce undercut along the sidewalls

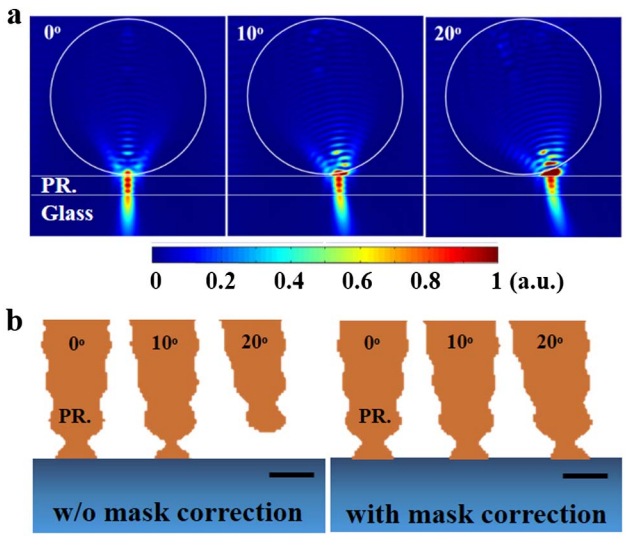

Fig. 3. (a) FDTD simulation (Lumerical) is performed to evaluate the formation of a photonic nanojet beneath the microsphere with different angles of incident. Microsphere has 2-μm diameter and photoresist (PR.) thickness is 280 nm. The substrate is glass. (b) Comparing the exposed-developed photoresist pillars through regulating the intensity of incident angle with and without modifying the mask sizes. The mask is only resized slightly to prevent the pillars from collapsing. The interference patterns along the vertical sides of pillars are due to mismatch between refractive indices of substrate and photoresist. Scale line is 100 nm.

of the photoresist pillars for lift-off process, it can limit the minimum feature size. The nodes of the resulted standing wave produce vulnerable spots on the photoresist pillar that sets a limit on the pillar's width, which beyond that, the pillar cannot survive during the developing process. One solution to address this problem is to implement an anti-reflection coating on the substrate to reduce the standing wave effect. Note that an arbitrary pattern contains photonic nanojet with different angle of incident. In our future work, we will consider an anti-reflection coating system composed of alternating layers of SiO_2 and Si_3N_4 thin films to suppress reflection. Another method to reduce the standing wave effect is to reduce the photoresist thickness. In this Letter, photoresist has a 280-nm thickness that can produce standing nodes due to interference between the upper and lower surfaces. A node close to the lower part of photoresist layer results in a vulnerable region on the photoresist pillar during the developing process. Here, the exposed-developed photoresist pillars are simulated for different angle of rays coming from macroscopic lens to analyze the effect of standing wave nodes and microsphere lens aberration as shown in Fig. 3(b). The simulation is derived from the calculation of electric field intensity of a photonic nanojet, which is normalized to the normal exposure angle and photoresist exposure-developing response. In addition, Fig. 3(b) compares the effect of modifying a mask to correct aberration of the microsphere lens. Note that without modifying the mask, high-angle pillars cannot survive. Thus, the pixels of mask are modified to regulate exposure power uniformly across a region with the sphere's radius approximately. The high aspect ratio (~3:1) of the pillars is quite favorable for a single-step pattern transfer process such as photoresist lift-off.

A semi-empirical graph of the relative opening size on the mask versus distance from center is shown in the inset of Fig. 4(a). Theoretical magnification of the imaging system is verified by comparing the distance of the openings on the modified mask and corresponding pillars in SEM. The background SEM shows a large area coverage of photoresist pillars with a corresponding modified mask. The process details of this fabrication can be found in Ref. [11]. The only differences are the photoresist thickness and the substrate. Here we used a glass slide as the substrate and chose 280-nm photoresist thickness to reduce interference effect based on FDTD simulation. We are planning to use anti-reflection coating for our future works, which is heavily studied [12] to produce smaller features. The inset SEM in Fig. 4(a) shows a coverage of ~1 μm width under the microsphere with a mean diameter of 2 μm. Outside of this coverage area cannot produce a well-defined photonic nanojet due to an extremely high angle and asymmetric boundary condition at the interface of the photoresist and air. As a rule of thumb, a controllable coverage area with a diameter of half of the sphere's diameter can be achieved by modifying the mask according to microsphere aberration and light illumination to mask nonuniformity. The number of pixels that can image with the proposed system is related to the nanopattern diameter under each sphere and the diameter of photoresist pillar $N_{\text{pixel}} = d_{\text{nano}}/2d_{\text{pillar}}$. For developing photoresist pillars on a glass substrate,

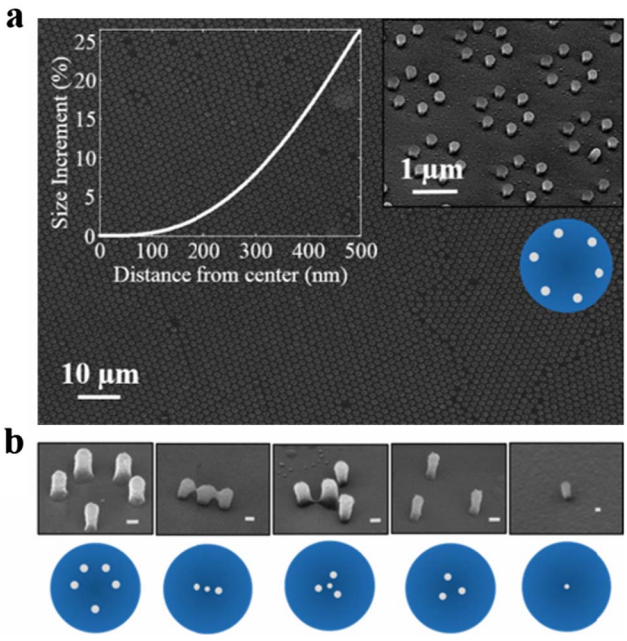

Fig. 4. (a) SEM of a hexagonal array of photoresist pillars that is produced by a mask that is shown in the lower right side of the figure. The zoom-in SEM shows few until cells of photoresist pillars. The graph on the upper left side of the figure shows the dependency of the mask openings on the exposure position under the microsphere. Pillars that are far from the center require larger power (equivalently larger opening size) to be survived during developing the photoresist. (b) SEM of different patterns of photoresist pillars with their corresponding modified masks. The scale bar is 100 nm.

simulated pillar's diameter is ~100 nm. In this Letter, we only consider 2-μm-diameter silica microspheres as they can generate photonic nanojet immediately below the sphere. Thus $d_{\text{nano}} \sim 1$ μm, resulting in 5 pixels in each direction. We have examined larger silica microspheres both in simulation and experiment to increase the number of pixels. However, larger spheres have less lens power due to reduction in sphere curvature as their photonic nanojet forms far below the photoresist region. One solution to adjust the relative position between the nanojet and photoresist for larger spheres is using spheres with higher refractive index such as Alumina and Titania that can compensate for lower sphere curvature and increasing the lens power. Another solution is to increase numerical aperture (NA) of the incident beam on the spheres by displacing the mask away from the focal point of the objective lens. However, our ray-tracing and lithography experiments demonstrate that the global coverage area is severely limited by high-NA-imaging beams due to the elevated aberration of the objective lens. Figure 4(b) shows SEM of different patterns of photoresist pillars with their corresponding modified masks. Note that all patterns have the same exposure time as their masks are modified to compensate for aberration and proximity. In addition, the interference patterns that are shown in Fig. 3(b) are suppressed in experimental results by increasing the exposure energy. We believe that by increasing the exposure energy, the intensity modulation along the sidewalls of the photoresist are shifted above the photoresist developing threshold and thus are not resolved.

In conclusion, we developed a DUV microsphere projection lithography to produce arbitrary nanopatterns with sub-100-nm feature size with 5 pixels in each lateral direction. The design procedure involves ray optics and wave optics as both macroscopic taking into account the proximity and aberration issues. The method is very suitable for large area defect-tolerable photonic structures and metasurfaces for energy harvesting, light extraction applications, and bio-sensing.

The authors would like to acknowledge partial support from NSF award no. ECCS-1310620, ARO award nos. W911NF-13-1-0485 and W911NF-11-1-0390. This work utilized Northwestern University Micro/Nano Fabrication Facility (NUFAB), which is supported by the State of Illinois and Northwestern University, as well as the high performance computational center (QUEST) at Northwestern University.

References

1. W. Wu, A. Katsnelson, O. G. Memis, and H. Mohseni, Nanotechnology **18**, 485302 (2007).
2. Y. C. Chang, S. C. Lu, H. C. Chung, S. M. Wang, T. D. Tsai, and T. F. Guo, Sci. Rep. **3**, 3339 (2013).
3. A. Bonakdar, S. J. Jang, and H. Mohseni, J. Vac. Sci. Technol. B **32**, 020604 (2014).
4. W. Guo, Z. B. Wang, L. Li, D. J. Whitehead, B. S. Luk'yanchuk, and Z. Liu, Appl. Phys. Lett. **90**, 243101 (2007).
5. S. Lecler, Y. Takakura, and P. Meyrueis, Opt. Lett. **30**, 2641 (2005).
6. D. Bothner, C. Clauss, E. Koroknay, M. Kemmler, T. Gaber, M. Jetter, M. Scheffler, P. Michler, M. Dressel, and D. Koelle, Appl. Phys. Lett. **100**, 012601 (2012).
7. W. P. Liyanage, J. S. Wilson, E. C. Kinzel, B. K. Durant, and M. Nath, Sol. Energy Mater. Sol. Cells **133**, 260 (2015).
8. Y. Zhang, T. Wei, Z. Xiong, Y. Chen, A. Zhen, L. Shan, Y. Zhao, Q. Hu, J. Li, and J. Wang, J. Appl. Phys. **116**, 194301 (2014).
9. K. Matsuyama, N. Ihsan, K. Irie, K. Mishima, T. Okuyama, and H. Muto, J. Colloid Interface Sci. **399**, 19 (2013).
10. T. Wei, K. Wu, D. Lan, Q. Yan, Y. Chen, C. Du, J. Wang, Y. Zeng, and J. Li, Appl. Phys. Lett. **101**, 211111 (2012).
11. A. Bonakdar, S. J. Jang, R. L. Brown, M. Rezaei, and H. Mohseni, Proc. SPIE **9170**, 917016 (2014).
12. T. Katayama, H. Motobayashi, W. B. Kang, M. A. Toukhy, J. E. Oberlander, S. S. Ding, and M. Neisser, Proc. SPIE **5377**, 968 (2004).